Supplemental Material for Visualization of Alternating Triangular Domains of Charge Density Waves in 2H–NbSe$_2$ by Scanning Tunneling Microscopy

Shunsuke Yoshizawa,[1,*] Keisuke Sagisaka,[1] and Hideaki Sakata[2]
[1]*Center for Basic Research on Materials, National Institute for Materials Science, 1-2-1 Sengen, Tsukuba, Ibaraki 305-0047, Japan*
[2]*Department of Physics, Tokyo University of Science, 1-3 Kagurazaka, Shinjuku, Tokyo 162-8601, Japan*
(Dated: October 27, 2023)

S1. POSSIBLE COMBINATIONS OF INDICES AND CORRESPONDING COMMENSURATE CDW STRUCTURES

In the main text, we model the topography of scanning tunneling microscopy (STM) by the sum of the local density of states (LDOS) from the crystal lattice and that from the charge density wave (CDW). It is expressed as

$$\rho^{(n_1,n_2,n_3)}(\mathbf{r}) = \rho_{\mathrm{Se}}(\mathbf{r}) + c\rho_{\mathrm{CDW}}^{(n_1,n_2,n_3)}(\mathbf{r}), \tag{S1}$$

The coefficient $c > 0$ is used to adjust the image contrast. We have selected $c \sim 2.5$ for our simulations. The LDOS from the crystal lattice, which reflects the locations of Se sites, is given by

$$\rho_{\mathrm{Se}}(\mathbf{r}) = \mathrm{Re}\sum_{j=1}^{3} \exp(i\mathbf{b}_j \cdot \mathbf{r}), \tag{S2}$$

while the LDOS from the CDW is given by

$$\rho_{\mathrm{CDW}}^{(n_1,n_2,n_3)}(\mathbf{r}) = \mathrm{Re}\sum_{j=1}^{3} \exp\left[i\left(\mathbf{Q}_j \cdot \mathbf{r} - \frac{2\pi}{3}n_j + \varphi_0\right)\right] \tag{S3}$$

with commensurate wavevectors $\mathbf{Q}_j = (1/3)\mathbf{b}_j$. The values of n_j ($j = 1, 2, 3$) control the positions of the CDW modulations relative to the crystal lattice. We can set a small phase offset φ_0 to adjust the appearance of simulated images, but we omit it for simplicity ($\varphi_0 = 0$). In commensurate CDW domains, n_j takes integer values, and the type of commensurate structure depends on $\lambda \equiv (n_1 + n_2 + n_3) \mod 3$. Specifically, when $\lambda = 0$, $\rho^{(n_1,n_2,n_3)}(\mathbf{r})$ reproduces the chalcogen-centered (CC) structure, where CDW maxima are located at chalcogen sites. When $\lambda = 1$, $\rho^{(n_1,n_2,n_3)}(\mathbf{r})$ reproduces the hollow-centered (HC) structure, where CDW maxima are at hollow sites. When $\lambda = 2$, the CDW maxima are at transition-metal sites, and the corresponding structure could be called the transition-metal-centered (TC) structure. However, this type of structure can be only accidentally found at the vertices of the CDW domains. The absence of the TC structure is probably beneficial in lowering the total energy, since density functional theory (DFT) calculations show that the formation energy of the TC structure is higher than that of the CC and HC structures [1]. The unit cell of the commensurate CDW contains nine chalcogen sites, nine hollow sites, and nine transition metal sites. Therefore, each of the CC, HC, and TC structures has nine variants that differ in phase and are distinguished by the label (n_1, n_2, n_3). All of these variants are illustrated in Fig. S1.

S2. FULL PROCEDURE TO DETERMINE CDW DOMAINS FROM TOPOGRAPHIC IMAGE

S2.1. Summary of Lawler–Fujita method

We summarize the method of extracting the displacement field of a periodic structure from a topographic image proposed by Lawler and Fujita *et al.* [2]. This method is essentially a lock-in technique with respect to the spatial coordinates. Let $z(\mathbf{r})$ be a topographic image that contains a periodic structure with a wavevector $\mathbf{q}$. The periodic structure may have a small strain, which is represented by a displacement field $\mathbf{u}(\mathbf{r})$. We can write the resulting topographic image as

$$z(\mathbf{r}) = z_0 \cos[\mathbf{q}\cdot(\mathbf{r}-\mathbf{u}(\mathbf{r}))] + \text{ other periodic components.} \tag{S4}$$

The key quantity in the Lawler–Fujita method is

$$C_{\mathbf{q}}(\mathbf{r}) \equiv \sum_{\mathbf{r}'} z(\mathbf{r}') \exp(-i\mathbf{q}\cdot\mathbf{r}') w(\mathbf{r}-\mathbf{r}'), \tag{S5}$$

where $w(\mathbf{r})$ is a normalized two-dimensional Gaussian function given by

$$w(\mathbf{r}) = \frac{1}{2\pi\sigma^2} \exp[-|\mathbf{r}|^2/(2\sigma^2)]. \tag{S6}$$

Since $C_{\mathbf{q}}(\mathbf{r})$ is the convolution of $z(\mathbf{r})\exp(-i\mathbf{q}\cdot\mathbf{r})$ and $w(\mathbf{r})$, it can be computed efficiently by using the fast Fourier transform. If σ is smaller than the length scale of the $\mathbf{u}(\mathbf{r})$ variation, we can approximate $C_{\mathbf{q}}(\mathbf{r})$ as

$$C_{\mathbf{q}}(\mathbf{r}) \simeq (z_0/2) \exp[-i\mathbf{q}\cdot\mathbf{u}(\mathbf{r})]. \tag{S7}$$

Hence, we can obtain information about $\mathbf{u}(\mathbf{r})$ from the phase factor

$$\varphi_{\mathbf{q}}(\mathbf{r}) \equiv \arg[C_{\mathbf{q}}(\mathbf{r})]. \tag{S8}$$

To remove the discreteness of $\varphi_{\mathbf{q}}(\mathbf{r})$ at $\pm\pi$, we must unwrap the phase to obtain a continuous function. The resulting quantity

---

[*] YOSHIZAWA.Shunsuke@nims.go.jp

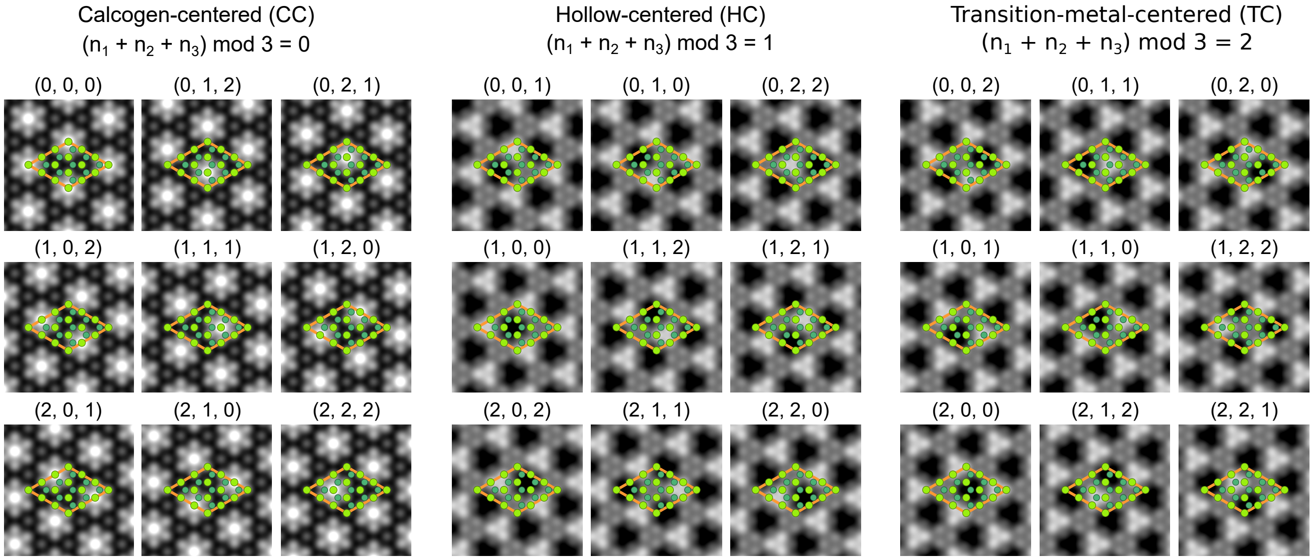

Fig. S1. Simulated topographic images of commensurate CDW structures labeled (n_1, n_2, n_3). The large dots in light green and small dots in green represent the Se and Nb sites, respectively. The orange rhombus in each image indicates the 3×3 cell of the CDW and is fixed to the atomic lattice to show the relative position of the CDW maxima.

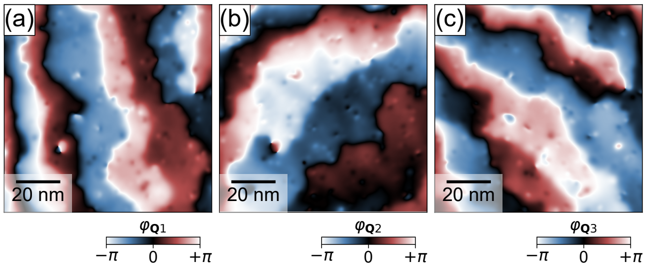

Fig. S2. (a)–(c) Images of $\varphi_{\mathbf{Q}_1}(\mathbf{r})$, $\varphi_{\mathbf{Q}_2}(\mathbf{r})$, and $\varphi_{\mathbf{Q}_3}(\mathbf{r})$ obtained from the topographic image in Fig. 2(a) of the main text.

provides the displacement field $\mathbf{u}(\mathbf{r})$ projected in the direction of $\mathbf{q}$,

$$\mathbf{q} \cdot \mathbf{u}(\mathbf{r}) = -\,\mathrm{unwrap}[\varphi_{\mathbf{q}}(\mathbf{r})]. \tag{S9}$$

We implemented the above procedure using the Python language. For two-dimensional phase unwrapping, we simply called the `skimage.restoration.unwrap_phase` function in the scikit-image library.

S2.2. Determination of intrinsic displacement field of CDW

Figures S2(a)–S2(c) shows the images of $\varphi_{\mathbf{Q}_j}(\mathbf{r})$ ($j = 1, 2, 3$) obtained by the Lawler–Fujita method from the topographic image in Fig. 2(a) of the main text. By unwrapping these phase images, we obtain the displacement field of the j-th CDW component projected to the direction of $\mathbf{Q}_j$, which is written as

$$u_j(\mathbf{r}) \equiv \mathbf{u}_j(\mathbf{r}) \cdot \mathbf{Q}_j/|\mathbf{Q}_j| = -\,\mathrm{unwrap}[\varphi_{\mathbf{Q}_j}(\mathbf{r})]/|\mathbf{Q}_j|. \tag{S10}$$

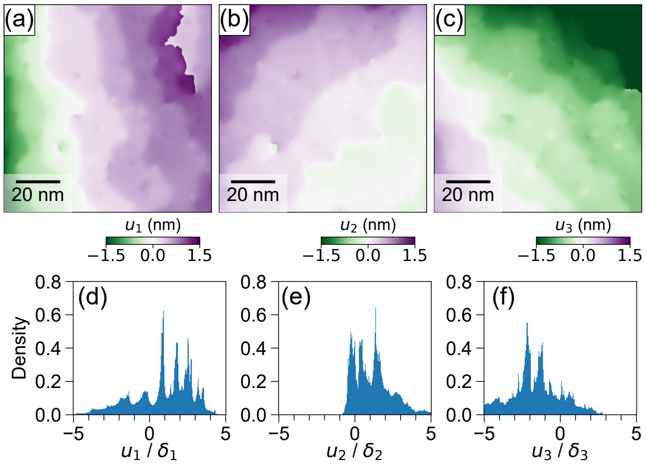

Fig. S3. (a)–(c) Images of $u_1(\mathbf{r})$, $u_2(\mathbf{r})$, and $u_3(\mathbf{r})$. (d)–(f) Histograms of $u_1(\mathbf{r})$, $u_2(\mathbf{r})$, and $u_3(\mathbf{r})$. The transverse axis is normalized by the interplanar spacing ($\delta_j \equiv 2\pi/|\mathbf{b}_j|$) to facilitate comparison with the histograms of $n_1(\mathbf{r})$, $n_2(\mathbf{r})$, and $n_3(\mathbf{r})$ in Fig. 3 in the main text. The vertical axis represents frequency density and is normalized so that the total area is 1.

The resulting images are shown in Figs. S3(a)–S3(c). Note that this displacement field is the sum of the intrinsic CDW displacements and the extrinsic image deformation due to the creep of the piezoelectric scanner of the STM head. Owing to the latter effect, the histograms of $u_1(\mathbf{r})$, $u_2(\mathbf{r})$, and $u_3(\mathbf{r})$ do not exhibit sharp peaks and contains a broad background, as shown in Figs. S3(d)–S3(f).

To eliminate the extrinsic image deformation, we measure the displacement field of the crystal lattice, denoted by $\mathbf{v}(\mathbf{r})$. Since the crystal lattice should have perfect periodicity, the

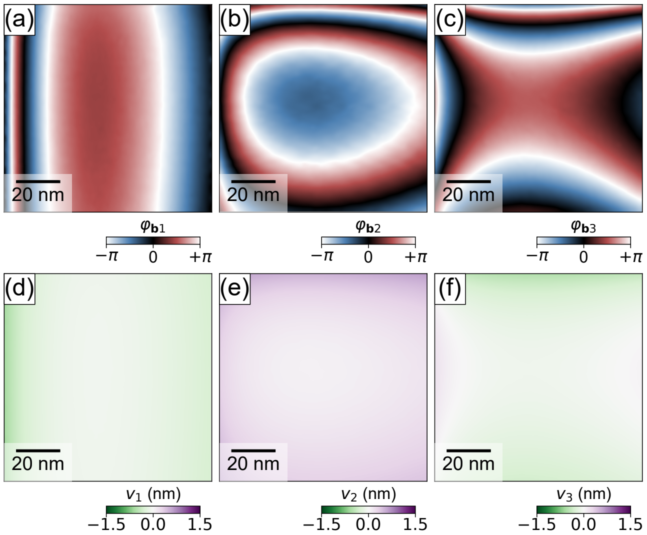

Fig. S4. (a)–(c) Images of $\varphi_{\mathbf{b}_1}(\mathbf{r})$, $\varphi_{\mathbf{b}_2}(\mathbf{r})$, and $\varphi_{\mathbf{b}_3}(\mathbf{r})$. (d)–(f) Images of $v_1(\mathbf{r})$, $v_2(\mathbf{r})$, and $v_3(\mathbf{r})$.

apparent displacement field of the crystal lattice in the topographic image is attributed purely to the extrinsic image deformation. By applying the Lawler–Fujita method to the periodicity of the crystal lattice, $\mathbf{b}_j$, we obtain the phase images, $\varphi_{\mathbf{b}_j}(\mathbf{r})$ [Figs. S4(a)–S4(c)], and the displacement fields, $v_j(\mathbf{r}) \equiv \mathbf{v}(\mathbf{r}) \cdot \mathbf{b}_j / |\mathbf{b}_j|$ [Figs. S4(d)–S4(f)]. The intrinsic displacement of the CDW can then be determined as

$$\delta u_j(\mathbf{r}) = u_j(\mathbf{r}) - v_j(\mathbf{r}). \tag{S11}$$

This argument, which assumes the perfect periodicity of the crystal lattice, may seem strange at first glance. For example, the CDW transition would be accompanied by lattice deformation at the same period as the CDW. Also, atomic defects could induce a local lattice distortion around them. However, the displacement field estimated by the Lawler–Fujita method is smoothed by a Gaussian window function characterized by σ. If σ is set sufficiently large, the lattice distortions mentioned above average out, because they are periodic or quite local. The insensitivity to local lattice distortions is verified by the smoothness of $\varphi_{\mathbf{b}_j}(\mathbf{r})$ and $v_j(\mathbf{r})$ shown in Fig. S4.

One might be concerned about the influence of the harmonics of the CDW on the determination of the displacement field of the crystal lattice, since the locations of the third-order Fourier peaks of the CDW coincide with those of the first-order peaks of the crystal lattice [Figs. 2(b) and 2(c) in the main text]. Such an influence can be neglected in the present case, because the contribution of the crystal lattice is dominant in the Bragg peaks. This is confirmed by the fact that the displacement fields determined for the periodicities $\mathbf{b}_1$–$\mathbf{b}_3$ are smooth functions, without any recognizable features related to the domain structure of the CDW. See $\varphi_{\mathbf{b}_j}(\mathbf{r})$ and $v_j(\mathbf{r})$ shown in Fig. S4.

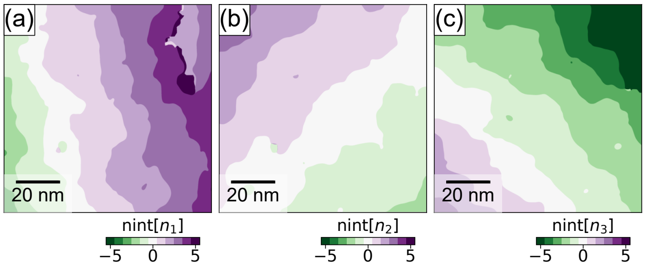

Fig. S5. (a)–(c) Images of nint[$n_1(\mathbf{r})$], nint[$n_2(\mathbf{r})$], and nint[$n_3(\mathbf{r})$].

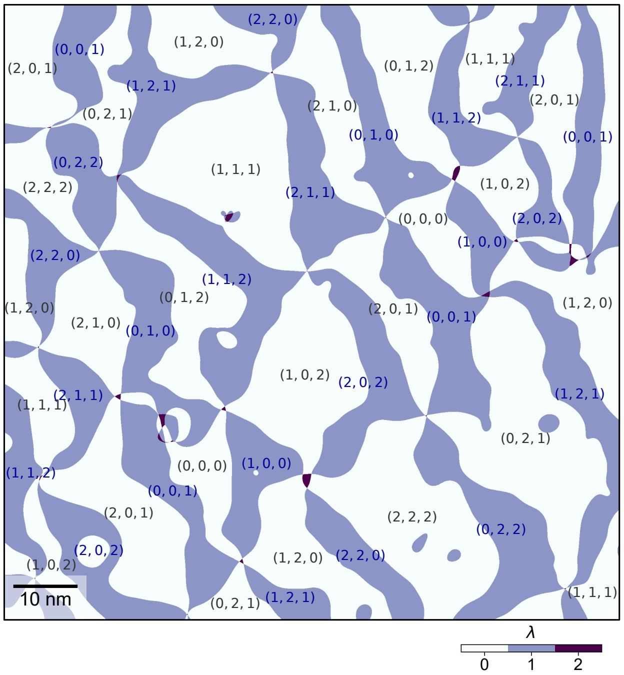

Fig. S6. (a)–(c)Image of $\lambda(\mathbf{r})$ of the same region studied in the main text. The CC and HC domains are depicted as white and blue areas, respectively. Each domain is labeled by reduced indices given by (n_1 mod 3, n_2 mod 3, n_3 mod 3).

S2.3. Determination of (n_1, n_2, n_3) and visualization of domain structure

By relating the intrinsic displacement field δu_j to the $(2\pi/3)n_j$ in Eq. (S3) and using $|\mathbf{Q}_j| = (1/3)|\mathbf{b}_j|$, we see that n_j can be calculated as

$$n_j(\mathbf{r}) = \frac{|\mathbf{b}_j|}{2\pi} \delta u_j(\mathbf{r}). \tag{S12}$$

Note that $|\mathbf{b}_j|/(2\pi)$ is the inverse of the interplanar spacing measured in the direction of $\mathbf{b}_j$. Figures 3(a)–3(c) of the main text display the obtained $n_1(\mathbf{r})$, $n_2(\mathbf{r})$, and $n_3(\mathbf{r})$. The corresponding histograms in Figs. 3(d)–3(f) exhibit sharp, equally spaced peaks at integers in contrast to the histograms obtained before subtracting the extrinsic deformation [Figs. S3(d)–

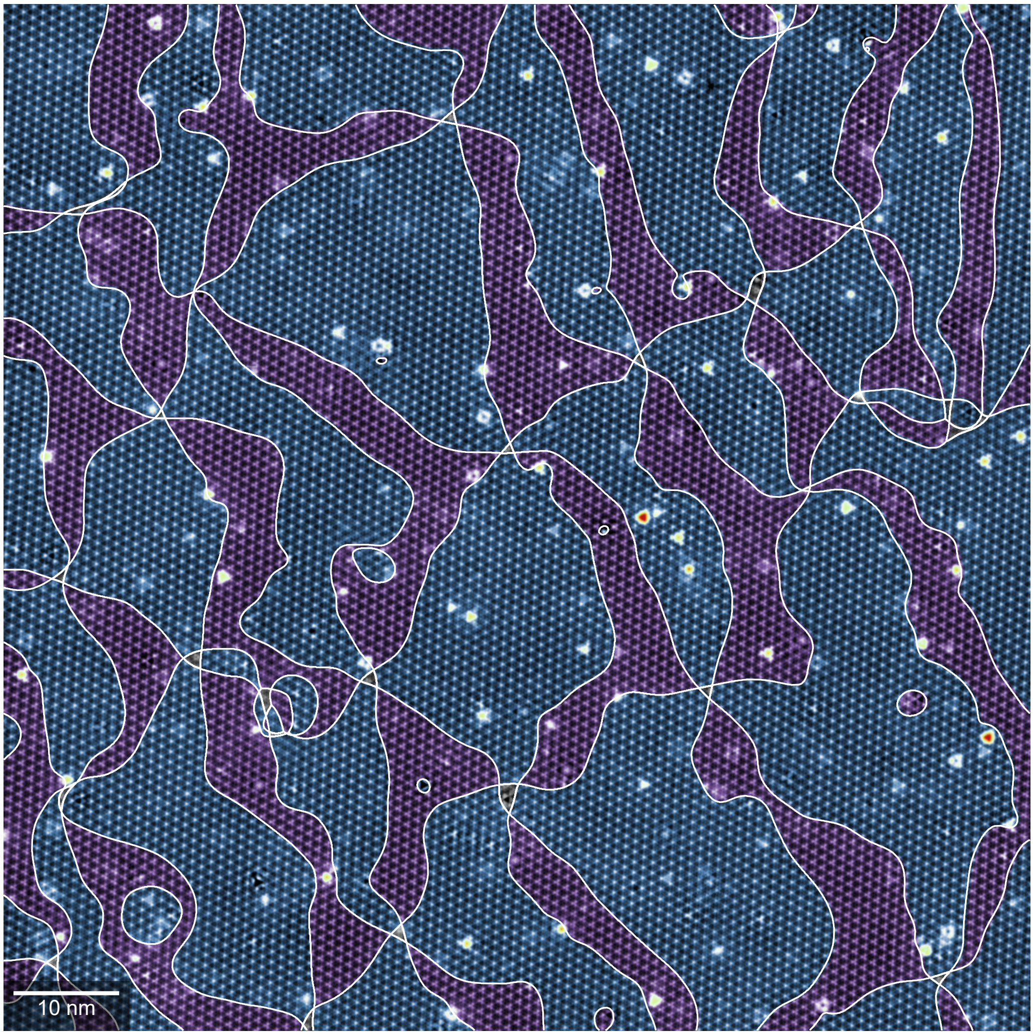

Fig. S7. Topographic image plotted with different colors corresponding to the domain type. The blue and purple areas correspond to the CC and HC regions, respectively. The original 2048 × 2048 pixels image was resampled to 1024 × 1024 pixels to reduce the file size.

S3(f)]. To visualize the domain structure, we define

$$\lambda(\mathbf{r}) \equiv \left\{ \sum_{j=1}^{3} \mathrm{nint}[n_j(\mathbf{r})] \right\} \bmod 3, \tag{S13}$$

where nint denotes the nearest integer. The images of $\mathrm{nint}[n_1(\mathbf{r})]$, $\mathrm{nint}[n_2(\mathbf{r})]$, and $\mathrm{nint}[n_3(\mathbf{r})]$ are shown in Figs. S5(a)–S5(c). The mapping of $\lambda(\mathbf{r})$, together with the triplet labels (n_1, n_2, n_3), is shown in Fig. 3(g) of the main text. Note that integers congruent modulo 3 can be considered equivalent as the label of the domains. For example, $(1, 0, -1)$ is equivalent to $(1, 0, 2)$, and the corresponding CDW images are identical. Considering this property, all of the CC and HC structures listed in Fig. S1 can be assigned to the observed domains. To illustrate this, in Fig. S6 we present the same domain structure as in Fig. 3(g) but labeled with reduced indices given by $(n_1 \bmod 3, n_2 \bmod 3, n_3 \bmod 3)$.

In Fig. S7, we present an atomically resolved topographic image plotted with different colors corresponding to values of λ to highlight the successful identification of the domain structure.

S2.4. Choice of the width of the Gaussian function

The value of σ was optimized by examining the balance between the resolution and smoothness. When we set $\sigma = 0.5$ nm, the detection of displacement fields is severely affected by the defects on the surface, as shown in Fig. S8(a). By setting larger σ values, the displacement field becomes smoother [Figs. S8(b)–S8(d)]. On the other hand, Table I indicates that the width of discommensurations is slightly overestimated when $\sigma = 1.5$ or 2 nm (see Section S3). We chose $\sigma = 1$ nm for our analysis, because the influence of surface defects is not significant and the estimated width of the discommensurate region remains to be as small as 3 nm.

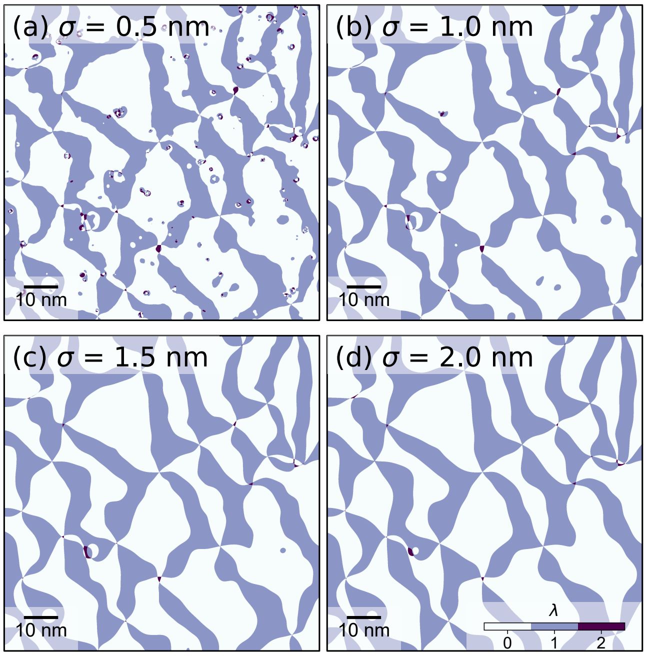

Fig. S8. (a)–(c) Domain images obtained with σ values of (a) 0.5 nm, (b) 1.0 nm, (c) 1.5 nm, and (d) 2.0 nm.

σ (nm)	d_1 (nm)	d_2 (nm)	d_3 (nm)	$\bar{d}$ (nm)
0.5	2.84	3.09	3.09	3.01
1.0	3.02	3.10	3.19	3.10
1.5	3.29	3.35	3.44	3.36
2.0	3.64	3.78	3.78	3.73

TABLE I. Discommensuration widths d_j and their average $\bar{d}$ estimated from the analyses with several choices of σ of the Gaussian used in the Lawler-Fujita method.

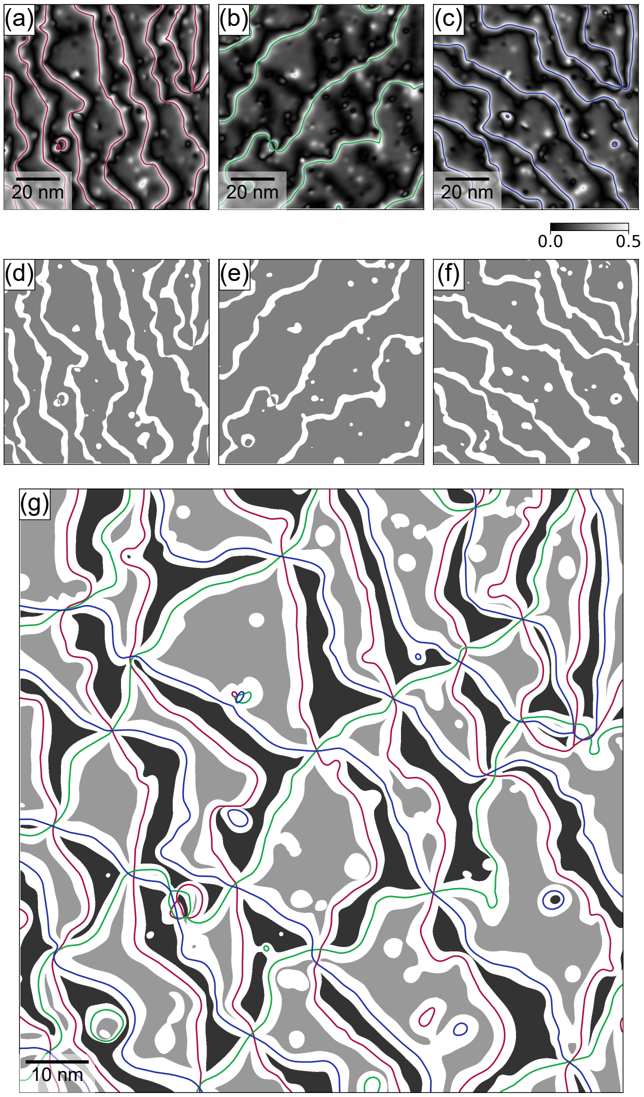

Fig. S9. (a)–(c) $\delta n_1(\mathbf{r})$, $\delta n_2(\mathbf{r})$, and $\delta n_3(\mathbf{r})$. The colored curves show the contours of $n_j(\mathbf{r})$ at half-integer values, illustrating discommensurations. (d)–(f) Maps of discommensurate regions. Areas where $\delta n_j(\mathbf{r}) > 0.25$ (≤ 0.25) are in white (gray). (g) Distribution of CC (gray region) and HC (black region) domains with discommensurate regions (white region) removed. The discommensurations determined from $n_1(\mathbf{r})$, $n_2(\mathbf{r})$, and $n_3(\mathbf{r})$ are depicted by curves in red, green, and blue, respectively.

S3. ANALYSIS OF DISCOMMENSURATE REGION

In the main text, we defined the discommensurate region as the region where $n_j(\mathbf{r})$ is closer to a half-integer than to an integer. To illustrate this region, we introduce the quantity $\delta n_j(\mathbf{r})$ given by

$$\delta n_j(\mathbf{r}) \equiv |n_j(\mathbf{r}) - \mathrm{nint}[n_j(\mathbf{r})]|, \tag{S14}$$

which varies between 0 in the middle of the commensurate domains and 0.5 along the discommensurations. Figures S9(a)–S9(c) display the images of $\delta n_j(\mathbf{r})$. The thick white wavy strips indicate that the phase jump occurs over a finite length. The red curves are the contours of $n_j(\mathbf{r})$ and provide the total length of the discommensuration, l_j. Figures S9(d)–S9(f) display the discommensurate region determined by the condition $\delta n_j(\mathbf{r}) > 0.25$, which provides the total area of the discommensurate region, A_j. We estimated the average width of the discommensuration of the j-th CDW component as $d_j = A_j/l_j$, which is shown in Table I. Since the σ of the Gaussian function used in the Lawler–Fujita method serves as a broadening factor, we examined the dependence of d_j on σ. Although the obtained d_j values increase with increasing σ, they are still smaller than σ, ensuring that the finite d_j is not an artifact. We believe that the intrinsic width of the discommensurate region is given by $d_j \simeq 3$ nm estimated for $\sigma = 0.5 - 1$ nm.

The finite width of the discommensuration does not affect the structural appearance of the domains. The formation of the alternating triangular domains reflects the phenomenon that the discommensurations in the three directions intersect at a single vertex. Since this phenomenon is independent of the width of the discommensurations, the triangular structure largely remains intact even when the discommensurate regions are explicitly depicted in the domain image [Fig. S9(g)].

S4. REPRODUCIBILITY CHECK ON ANOTHER SAMPLE

We have confirmed the observation of the triangular domains of CDW for STM images of different regions of the same sample, as well as for STM images of several $2H$–NbSe$_2$ samples. As evidence of the reproducibility, we show the analysis of the CDW domains on a $2H$–NbSe$_2$ crystal purchased from HQ Graphene [Fig. S10]. The analysis was done for a topographic image of a 150 nm x 150 nm region [Fig. S10(a)]. The Fourier transform resolves peaks of CDW and crystal lattice [Fig. S10(b)]. The images cropped from regions labeled A and B in Fig. S10(a) shows typical CC and HC structures [Figs. S10(c) and S10(d)] and their Fourier amplitude images are nearly identical [Figs. S10(e) and S10(f)]. By applying the domain visualization method proposed in our study, we obtained the domain structure shown in Fig. S10(g). Most of the region is occupied by alternating triangular domains, supporting our main finding. The images of $n_1(\mathbf{r})$, $n_2(\mathbf{r})$, and $n_3(\mathbf{r})$ used to generate the domain image exhibit step-terrace structures [Figs. S10(h)-S10(j)]. Their histograms display sharp peaks at integer multiple of the interplanar spacing [Figs. S10(k)-S10(m)]. Figs. S10(h)-S10(j) also reveals the locations of topological defects as indicated by arrows. One can confirm that the topological defects are created in pairs in two of the three CDW components.

S5. NUMERICAL SIMULATION OF CDW DOMAIN STRUCTURE BASED ON EMPIRICAL FREE ENERGY

S5.1. Free energy for single-layer transition-metal dichalcogenides

Nakanishi and Shiba proposed a free energy expression to describe the CDW transition of transition-metal dichalcogenides (TMDCs) [3, 4]. The CDW is characterized by an incommensurate wavevector $\mathbf{Q}_j^{\mathrm{IC}}$ that is close to $\mathbf{Q}_j = \mathbf{b}_j/3$. The order parameter $\phi_j(\mathbf{r})$ is a complex-valued function chosen so that the charge density attributed to the CDW is

$$\rho_{\mathrm{CDW}}(\mathbf{r}) = \mathrm{Re} \sum_{j=1}^{3} e^{i\mathbf{Q}_j\cdot\mathbf{r}} \phi_j(\mathbf{r}). \tag{S15}$$

We use the notation $\phi_{j+3} = \phi_j$. The free energy $F(\phi_1, \phi_2, \phi_3)$ is given by

$$F(\phi_1, \phi_2, \phi_3) = \int \mathrm{d}\mathbf{r} \Bigg\{ \sum_{j=1}^{3} \Big[(T - T_{\mathrm{CDW}})|\phi_j|^2 + s\left|\left(-i\nabla - \mathbf{q}_j\right)\phi_j\right|^2 + B|\phi_j|^4 + C|\phi_j|^2|\phi_{j+1}|^2 + \\ + \mathrm{Re}(Y e^{\pm iy}\phi_j^3 + W e^{\pm iw}\phi_j^2\phi_{j+1}^*\phi_{j+2}^*) \Big] + \mathrm{Re}(D e^{\pm id}\phi_1\phi_2\phi_3) \Bigg\}, \tag{S16}$$

where $\mathbf{q}_j \equiv \mathbf{Q}_j^{\mathrm{IC}} - \mathbf{Q}_j$, T is the temperature, T_{CDW} is the CDW transition temperature, and B and C are real parameters. The terms with Y and W are commensurability energies that regulate the phase between the CDW components, while the term with D is the phase term, which adjusts the phase relation between the CDW and the crystal lattice. The ± signs in the terms with Y, W, and D correspond to the even layer (+) and odd layer (−) of the $2H$ structure. The crystal structure of the surface layer used in our study [Fig. 1(a) of the main text] corresponds to the odd layer in their definition. The free energy of bulk TMDCs has an additional term for the interaction between layers. The relative stability of the three types of commensurate structure depends on the parameters y, w, and d. The condition where the CC and HC structures become equally stable is obtained by setting $y = w = 0$ and $d = \pi$.

Note that in the Nakanishi–Shiba papers, the origin of the spatial coordinates is considered to be a transition metal site, which differs from our convention. In addition, their definition of the indices n_1, n_2, and n_3 labeling the domains has the opposite sign to our definition of n_1, n_2, and n_3. As a result, $\lambda = (n_1 + n_2 + n_3) \mod 3$ also has the opposite sign. Consequently, the domains labeled $\lambda = 0$, 1, and 2 in their papers correspond to the TC, HC, and CC structures, respectively.

We employed a time-dependent Ginzburg-Landau approach to minimize the free energy. The variation of F with respect to ϕ_j^* is given by

$$\frac{\delta F}{\delta \phi_j^*} = (T - T_c)\phi_j + s\left(-i\nabla - \mathbf{q}_j\right)^2 \phi_j + 2B|\phi_j|^2\phi_j + C\phi_j(|\phi_{j+1}|^2 + |\phi_{j+2}|^2) + \frac{3}{2} Y e^{\mp iy}\phi_j^{*2} + \\ + \frac{1}{2} W e^{\mp iw} 2\phi_j^*\phi_{j+1}\phi_{j+2} + \frac{1}{2} W e^{\pm iw}(\phi_{j+1}^2\phi_{j+2}^* + \phi_{j+2}^2\phi_{j+1}^*) + \frac{1}{2} D e^{\mp id}\phi_{j+1}^*\phi_{j+2}^*. \tag{S17}$$

This provides the time evolution of the free energy [5, 6],

$$\frac{\partial \phi_j}{\partial t} = -\frac{\delta F(\phi_1, \phi_2, \phi_3)}{\delta \phi_j^*}. \tag{S18}$$

We computed the time evolution of ϕ_j using this equation until

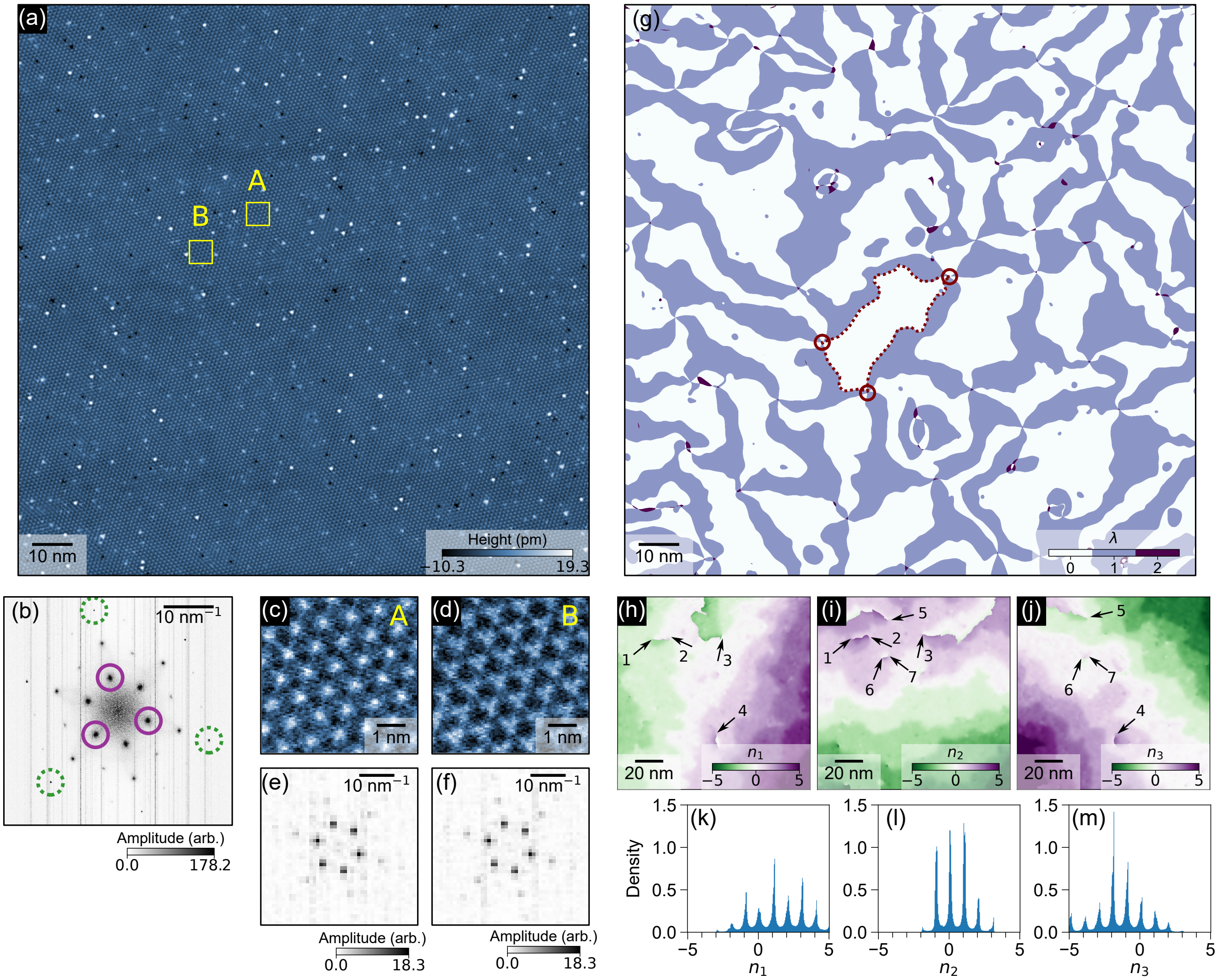

Fig. S10. (a) Topographic image of a 150 nm × 150 nm area of a cleaved surface of a 2H–NbSe$_2$ crystal purchased from HQ Graphene. The data were recorded at a resolution of 1024 × 1024. The image was flattened by subtracting a third-order polynomial fit from each line to remove the slope and a small curvature. The feedback condition was 100 pA at 50 mV. (b) Fourier transform of the topographic image in (a). The dotted and solid circles indicate the spots of the atomic lattice and those of the CDW, respectively. (c) and (d) Cropped images of the CC and HC domains indicated by the boxes labeled A and B in (a). (e) and (f) Fourier transform images of cropped data of (c) and (d). (g) Image of $\lambda(\mathbf{r})$. The CC and HC domains are depicted as white and blue areas, respectively. The circles and dotted curves are the vertices and edges of one of a CC domain, respectively. (h)–(j) Images of $n_1(\mathbf{r})$, $n_2(\mathbf{r})$, and $n_3(\mathbf{r})$, which were obtained from the topographic data in (a) and were used to calculate the domain structure in (g). The arrows indicate the locations of topological defects. Each pair of topological defects at the same location but in different CDW components is labeled with the same number. (k)–(m) Histograms of $n_1(\mathbf{r})$, $n_2(\mathbf{r})$, and $n_3(\mathbf{r})$. The vertical axis represents the frequency density.

the change in F became sufficiently small. We used the split-operator Fourier method to handle the terms involving spatial derivatives in the reciprocal space. The calculations were performed on a 1024 × 1024 grid over a $300a \times 300a$ area (a is the lattice constant). The parameters used in the computation are $\mathbf{q}_j = -0.025\mathbf{Q}_j$, $s = 1000$, $T_{\mathrm{CDW}} = 1$, $T = 0.87$, $B = 2$, $C = 1$, $D = 0.2$, $Y = 0.45$, $W = 1$, $y = w = 0$, and $d = \pi$. These parameters are the same as those used in Ref. [4].

Figures S11(a)-S11(c) and S11(d)-S11(f) show the phase and amplitude of $\phi_j(\mathbf{r})$, respectively. In discommensurations, $\arg[\phi_j(\mathbf{r})]$ changes abruptly, and $|\phi_j(\mathbf{r})|$ is locally suppressed. Since we set $\phi_j = 0$ as the boundary condition, the resulting $\phi_j(\mathbf{r})$ is distorted near the boundary. The topographic image is simulated as a weighted sum of $\rho_{\mathrm{Se}}(\mathbf{r})$ and $\rho_{\mathrm{CDW}}(\mathbf{r})$ given by Eqs. (S2) and (S15), respectively, with an appropriate adjustment of the origin of the spatial coordinates. The triplet (n_1, n_2, n_3) is obtained from $\arg[\phi_j(\mathbf{r})]$, and the domain type is distinguished from the λ computed from the triplet. Figure 4(a) in the main text is a combined plot of the simulated topographic image and the domain structure in a region cropped near the center where the distortion of $\phi_j(\mathbf{r})$ due to the boundary effect is negligible.

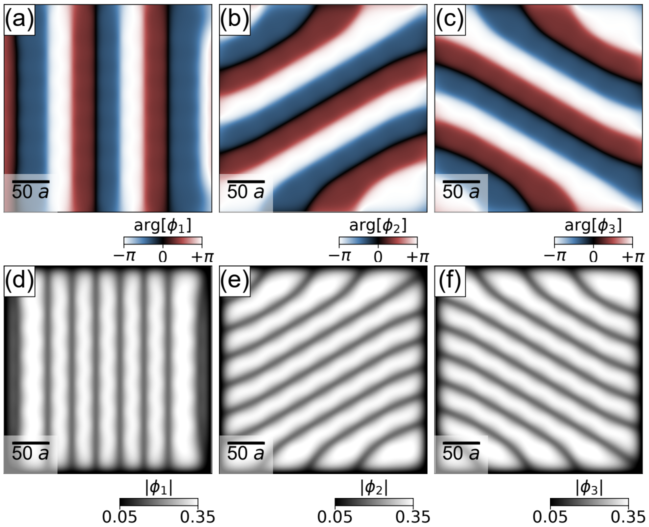

Fig. S11. Order parameters obtained by minimizing Nakanishi-Shiba's free energy. (a)–(c) Images of arg[$\phi_1(\mathbf{r})$], arg[$\phi_2(\mathbf{r})$], and arg[$\phi_1(\mathbf{r})$]. (d)–(f) Images of $|\phi_1(\mathbf{r})|$, $|\phi_2(\mathbf{r})|$, and $|\phi_3(\mathbf{r})|$.

[1] G. Gye, E. Oh, and H. W. Yeom, Topological landscape of competing charge density waves in 2*H*–NbSe$_2$, Phys. Rev. Lett. **122**, 016403 (2019).

[2] M. J. Lawler, K. Fujita, J. Lee, A. R. Schmidt, Y. Kohsaka, C. K. Kim, H. Eisaki, S. Uchida, J. C. Davis, J. P. Sethna, and E.-A. Kim, Intra-unit-cell electronic nematicity of the high-tc copper-oxide pseudogap states, Nature (London) **466**, 347 (2010).

[3] K. Nakanishi and H. Shiba, Theory of discommensurations and re-entrant lock-in transition in the charge-density-wave state of 2H-TaSe$_2$, J. Phys. Soc. Jpn. **52**, 1278 (1983).

[4] H. Shiba and K. Nakanishi, Phenomenological Landau theory of charge density wave phase transitions in layered compounds, in *Structural Phase Transitions in Layered Transition-metal Compounds*, edited by K. Motizuki (D. Reidel, 1986) pp. 175–266.

[5] A. J. Bray, Theory of phase-ordering kinetics, Adv. Phys. **51**, 481 (2002).

[6] S. Vogelgesang, G. Storeck, J. G. Horstmann, T. Diekmann, M. Sivis, S. Schramm, K. Rossnagel, S. Schäfer, and C. Roper, Phase ordering of charge density waves traced by ultrafast low-energy electron diffraction, Nat. Phys. **14**, 184 (2017).